A Novel Label-Free EC Aptasensor for Early Detection of H9N2 Influenza Using FFT-square wave voltammetry and Validated by Molecular Docking

Negar Heidari[1,2], Nogol D. Moghaddam[2], Sharmin Kharrazi[3], Jahan B. Ghasemi[2,], Melika F. Aghdam[2], Mahdi Amrollahi Bioyki[1] , Ebrahim Ghafar-Zadeh[1*], and Parviz Norouzi[1,2*]

[1] Dept. of Electrical Engineering and Computer Science, Lassonde School of Engineering, York University, Toronto, Canada

[2] School of Chemistry, University College of Science, University of Tehran, P.O. Box 14155-6455, Tehran, Iran

[3] Department of Medical Nanotechnology, School of Advanced Technologies in Medicine, Tehran University of Medical Sciences, Tehran, Iran

Corresponding Author: Parviz Norouzi, Email: **pnorouzi@yorku.ca**

1. SI-1. Measurement Methodology in FFT Voltammetry (FFTSWV)

Square-wave voltammetry (SWV) is a highly sensitive electroanalytical technique in which a square-wave potential is superimposed on a staircase or linear potential ramp to probe electrochemical systems. In the present work, a modified frequency-domain implementation of SWV was employed to enhance signal discrimination and analytical sensitivity. The applied potential waveform, illustrated in Fig. S1A, consists of a small-amplitude square wave superimposed on a linear potential ramp and is described by Eq. S1:

$$E_{SW}(t) = \Delta E(\omega t) + vt \qquad \text{(Eq. S1)}$$

where ΔE is the square-wave amplitude, ω is the angular frequency of the applied waveform (ω = 2πf), and v is the linear potential scan rate[1].

The resulting electrode current response contains multiple harmonic components arising from the nonlinear characteristics of the electrochemical interface and can be expressed as a Fourier series:

$$I_{ac}(t) = \Delta I_1 cos(\omega t + \phi_1) + \Delta I_2 cos(2\omega t + \phi_2) + \Delta I_3 cos(3\omega t + \phi_3) + \cdots \qquad \text{(Eq. S2)}$$

where ΔI represents the amplitude of the square-wave current, φ denotes the phase shift relative to the applied potential, and the subscripts correspond to the harmonic order of the electrode response[2].

Although the harmonic frequencies in Eq. S2 originate from nonlinear electrochemical processes, the experimental conditions adopted in this study maintain the electrode–solution interface in a

quasi-linear regime. This allows reliable harmonic decomposition while minimizing distortion of the fundamental electrochemical response. The first term in Eq. S2 represents the fundamental component of the current, oscillating at the same frequency as the applied square-wave potential and containing the primary Faradaic information of the system.

As shown in Fig. S1B, FFT-SWV employs a more comprehensive data acquisition strategy than conventional SWV. Instead of sampling the current at only two points per square-wave cycle, the current is sampled eight times during each cycle (t_0–t_7). These samples are processed using a discrete Fast Fourier Transform (FFT), where the number of sampled points must be a power of 2 (2^n) to satisfy FFT computational requirements.

Accordingly, the sampled currents (I_{ns}) are acquired at uniform time intervals defined as:

$$t_s,\ t_s + \frac{1}{8f_0},\ t_s + \frac{2}{8f_0},\ \ldots,\ t_s + \frac{7}{8f_0}$$

where f_0 is the fundamental square-wave frequency. For each potential increment (ΔE) in the ramp, Nc square-wave cycles are applied, yielding a total of 8Nc current samples (I_0–I_7 for each cycle). Thus, the complete time-domain dataset for each ΔE consists of Nc × 8 current values.

These data are transformed into the frequency domain using discrete FFT calculation, generating a complex series of frequency components (f_n) that represent the fundamental and higher harmonic contributions of the electrode response. At the end of each potential step, the FFT-processed data are stored in an array matrix as:

$$\text{Data arry} = \begin{pmatrix} I_0^1 & \ldots. & I_3^1 \\ . & . & . \\ I_0^{Nct} & \ldots & I_3^{Nct} \end{pmatrix} \qquad \text{(Eq. S3)}$$

Subsequent digital filtering and signal reconstruction yield the time-domain current according to [3]:

$$I_t = \sum_{n=0}^{N-1} [F_n cos(\frac{2\pi t}{N}) + jF_n sin(\frac{2\pi t}{N})] \qquad \text{(Eq. S4)}$$

where N represents the total number of current data points collected during the experiment. By transforming the electrochemical response into the frequency domain, FFT-SWV enables selective isolation of Faradaic signal components while effectively suppressing capacitive background currents and low-frequency noise. Compared to conventional time-domain SWV, this approach significantly improves the signal-to-noise ratio, enhances measurement resolution, and increases analytical sensitivity—particularly in complex matrices where baseline drift and non-specific contributions can obscure the true electrochemical response[4].

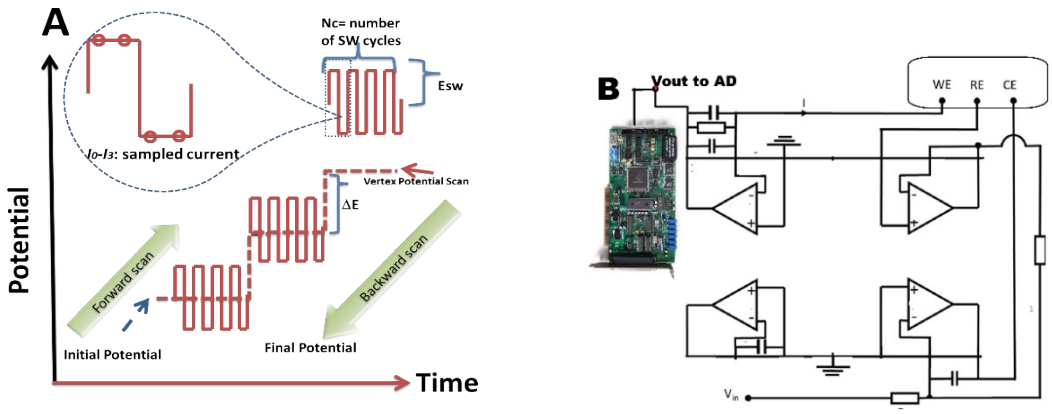

Figure S1. A) Schematic diagram illustrates the applied potential waveform, square wave potentials superimposition each step of the potential ramp. SW potential cycle/ the currents were sampled 4 times, **B)** Schematic of the Potentiostat Circuit diagram for FFTSWV measurements.

The FFT-SWV signals recorded in phosphate-buffered saline (PBS) in the presence of the analyte are shown in Fig. S2. All FFT-SWV voltammograms were subjected to consistent digital processing steps, including FFT-based smoothing and background correction, ensuring reliable comparison across measurements. Overall, this frequency-domain SWV framework provides a robust and information-rich methodology for electrochemical biosensing, offering clear advantages over conventional voltammetric techniques in terms of sensitivity, noise suppression, and interpretability of interfacial electrochemical behavior

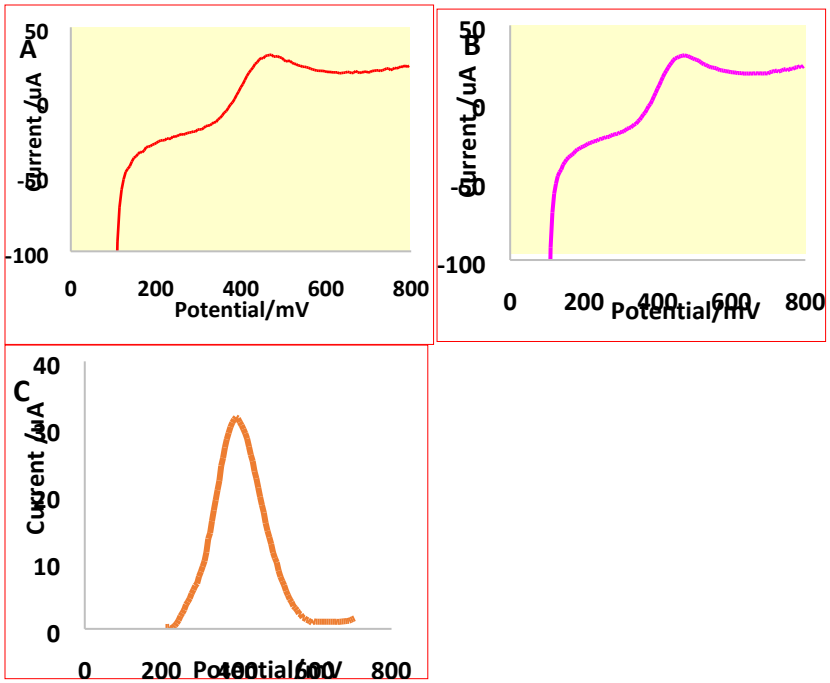

Figure S2. The FFT differential admittance voltammograms for the optimization of frequency and amplitude for FFTSWV in solution of PBS pH 7.5, at frequency of 177 Hz, and amplitude range of 20 mV, \number of cycles SW set to 127, and a potential range of 100 to 700 mV. The voltammograms A (origal), B) FFT smoothing, C) background correction.

SI-2. Electron microscopy and EDX Analysis and maps

Field-emission scanning electron microscopy (FE-SEM) combined with energy-dispersive X-ray spectroscopy (EDS) was employed to investigate the morphology, elemental composition, and spatial distribution of materials at each intermediate stage of electrode modification prior to AuNP deposition. For each electrode configuration, the EDS spectrum with the associated quantitative elemental percentages is first discussed, followed by the corresponding elemental mapping results presented within the same figure. For the pristine gold electrode, the EDS spectrum (Fig. S3A) shows a dominant Au signal exceeding 99 wt%, confirming the high purity of the metallic substrate and the absence of detectable impurities. The corresponding elemental map (Fig. S3B) reveals a uniform gold distribution across the entire electrode surface, indicating a homogeneous and continuous Au layer without compositional heterogeneity.

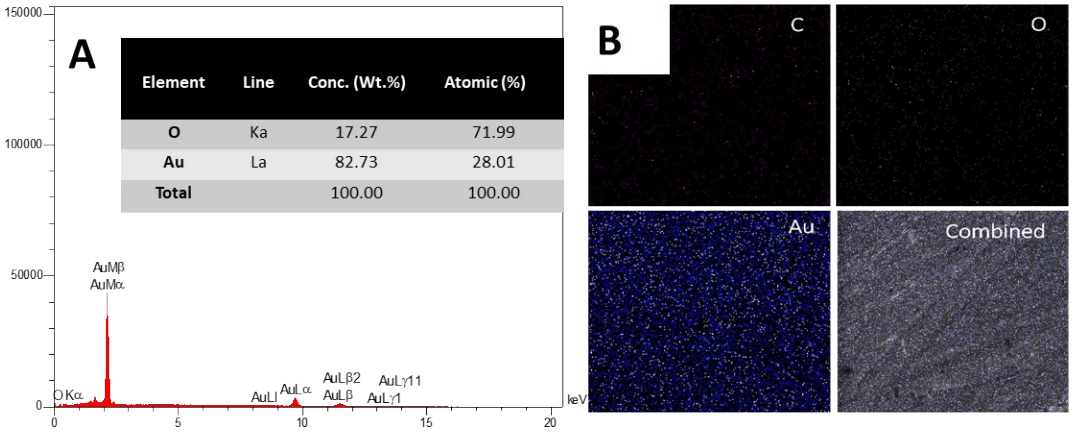

Fig. S3. EDX Analysis and maps of AuE.

After graphene oxide deposition, the EDS spectrum (Fig. S4A) reveals the emergence of carbon and oxygen as the predominant elements, while the Au signal is substantially attenuated, confirming effective surface coverage by GO sheets. The quantitative composition extracted from the EDS spectrum indicates that carbon and oxygen together account for the majority of the detected elements, consistent with oxygen-rich graphene oxide. The accompanying elemental maps (Fig. S4B) show a homogeneous spatial distribution of both carbon and oxygen over the electrode surface, confirming continuous GO film formation without exposed gold regions.

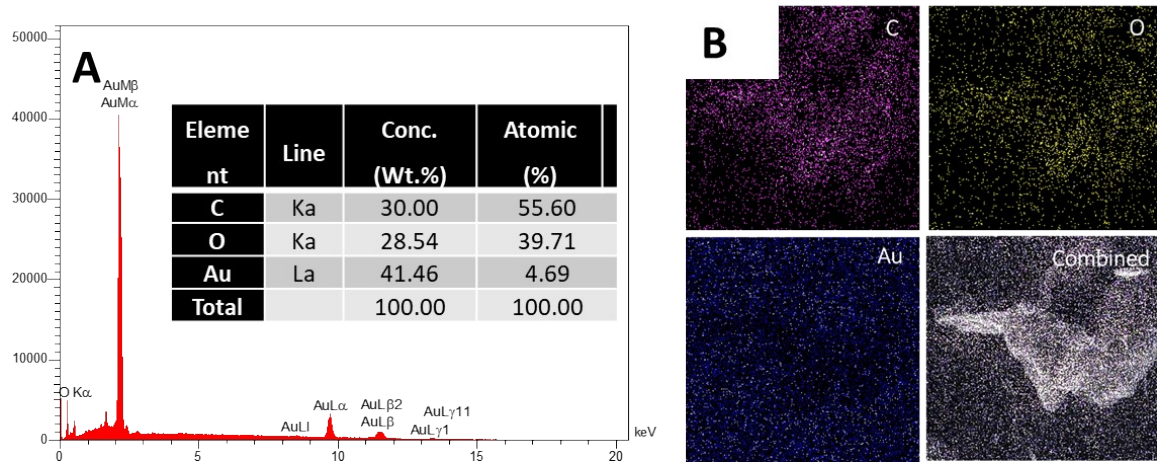

Fig. S4. EDX Analysis and maps of AuE/GO.

Upon incorporation of cerium oxide nanoparticles, the EDS spectrum (Fig. S5A) displays distinct cerium peaks together with an increased oxygen contribution, reflecting the presence of CeO_2 in addition to GO oxygen functionalities. Quantitative analysis extracted directly from the EDS spectrum indicates a measurable cerium content with low variation across analyzed regions. The corresponding elemental maps (Fig. S5B) demonstrate strong spatial co-localization of Ce, O, and C signals throughout the electrode surface, confirming uniform dispersion of CeO_2 nanoparticles within the GO matrix rather than localized aggregation. The low relative deviation (<7%) in cerium and oxygen content across mapped areas further indicates good compositional uniformity. This intercalated CeO_2–GO architecture is consistent with previous reports showing that cerium oxide nanoparticles embedded within graphene-based matrices suppress sheet restacking, introduce oxygen-vacancy-rich interfaces, and enhance interfacial stability and charge-transfer pathways.

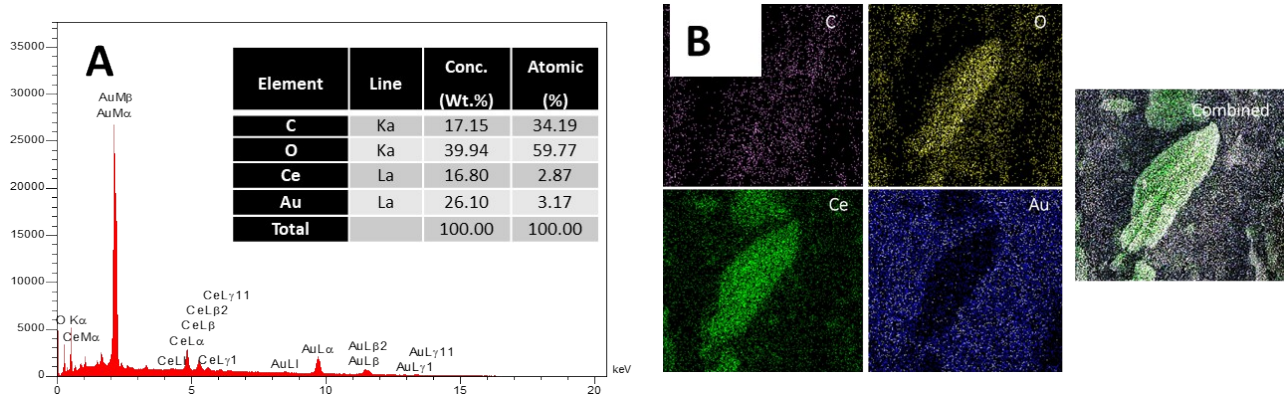

Fig. S5. EDX Analysis and maps of AuE/nanoCeO_2-GO.

Overall, the combined FE-SEM morphology, EDS-derived quantitative compositions, and elemental mapping analyses presented in Figs. S3–S5 confirm the controlled and reproducible fabrication of the AuE, AuE/GO, and AuE/nanoCeO_2–GO electrodes, providing a structurally and compositionally validated foundation for the final AuNP-modified sensing interface discussed in the main text.

SI-3. EC characterization of the aptasensor

The stepwise modification of the electrode was confirmed by cyclic voltammetry, showing successive changes in redox current and peak separation consistent with surface functionalization,

figure S6. In particular, nanocomposite formation enhanced electron transfer, while aptamer immobilization and subsequent virus binding led to progressive current suppression due to electrostatic effects, surface blocking, and steric hindrance of the redox probe.

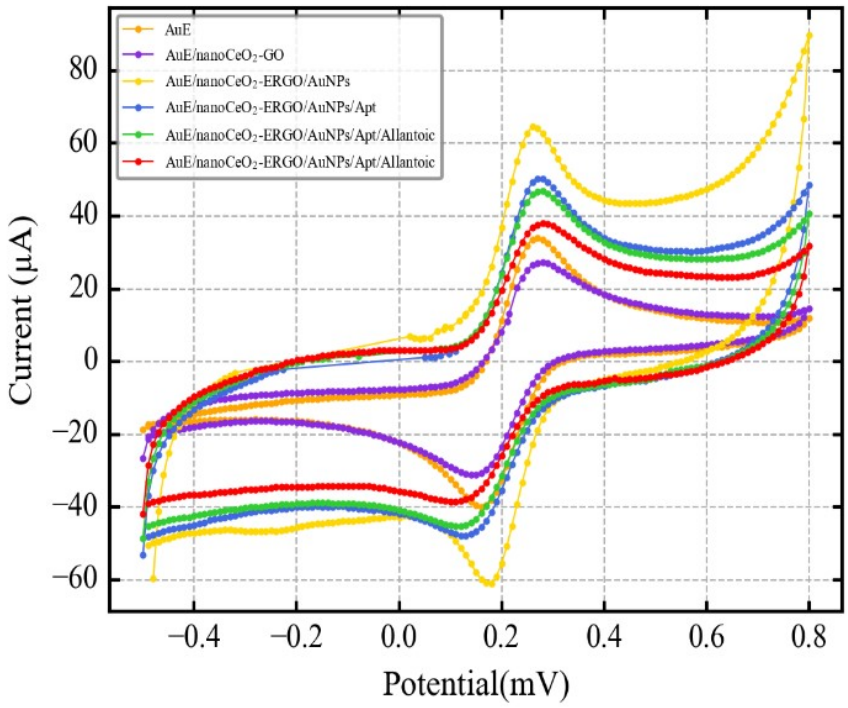

Figure S6. CVs of (a) bare Au (b) Au/nanoCeO$_2$-GO (c) Au/nanoCeO$_2$-rGO/AuNPs (d) Au/nanoCeO$_2$-rGO/AuNPs/Apt (e) Au/nanoCeO$_2$-rGO/AuNPs/ Apt/Allantoic (f) Au/nanoCeO$_2$-rGO/ AuNPs/Apt/Allantoic/H9N2 in 0.1 M PBS solution, pH 7.5 containing 5 mmol L^{-1} $[Fe(CN)_6]^{3-/4-}$ and 250 mmol L^{-1} KCl,

SI-4. Optimization of EC parameters

In FFT-SWV measurements, the square-wave frequency, amplitude, and number of cycles collectively define the effective potential sweep rate experienced by the electrochemical system, in close analogy to scan-rate control in cyclic voltammetry. Consequently, optimization of these parameters is essential to balance Faradaic charge transfer against kinetic and capacitive limitations at the electrode–electrolyte interface. As shown in Fig. S7, increasing the square-wave frequency from 88 to 177 Hz enhances the electrochemical response, reflecting an increase in the

effective sweep rate that remains compatible with the fast and reversible redox kinetics of the $[Fe(CN)_6]^{3-/4-}$ couple at the modified electrode surface[49, 50]. Within this regime, electron transfer and ion transport can adequately follow the applied potential modulation, leading to enhanced Faradaic current. At higher frequencies, however, the effective sweep rate becomes excessive, analogous to operating cyclic voltammetry at overly high scan rates. Under these conditions, the characteristic time scale of the excitation approaches or exceeds the intrinsic charge-transfer and mass-transport time constants, resulting in incomplete redox conversion, increased capacitive contributions, and distortion of the FFT-SWV response[37]. This kinetic mismatch leads to a progressive attenuation of the Faradaic signal and reduced analytical performance. A similar trade-off is observed for the square-wave amplitude. Increasing the amplitude up to 20 mV improves sensitivity by increasing the driving force for electron transfer, whereas larger amplitudes introduce non-ideal electrochemical behavior, including elevated capacitive currents and degradation of the signal-to-noise ratio. The influence of the number of square-wave cycles (N_sw) on the FFT-SWV response is shown in Fig. 6B. Increasing N_sw from 16 to 120 cycles leads to a progressive enhancement of the Faradaic signal, attributed to improved signal averaging while maintaining a sufficiently high effective sweep rate. In this regime, charge-transfer kinetics remain favorable and the cumulative Faradaic contribution increases. At higher N_sw values (256 cycles), the response decreases markedly. This behavior arises from a reduction in the effective sweep rate (Eq. S1), analogous to excessively slow scan rates in cyclic voltammetry, where diffusion and capacitive contributions dominate and attenuate the Faradaic signal. Based on the combined optimization of frequency, amplitude, and cycle number, 177 Hz, 20 mV, and N_sw = 120 were selected as the optimal FFT-SWV conditions for subsequent measurements.

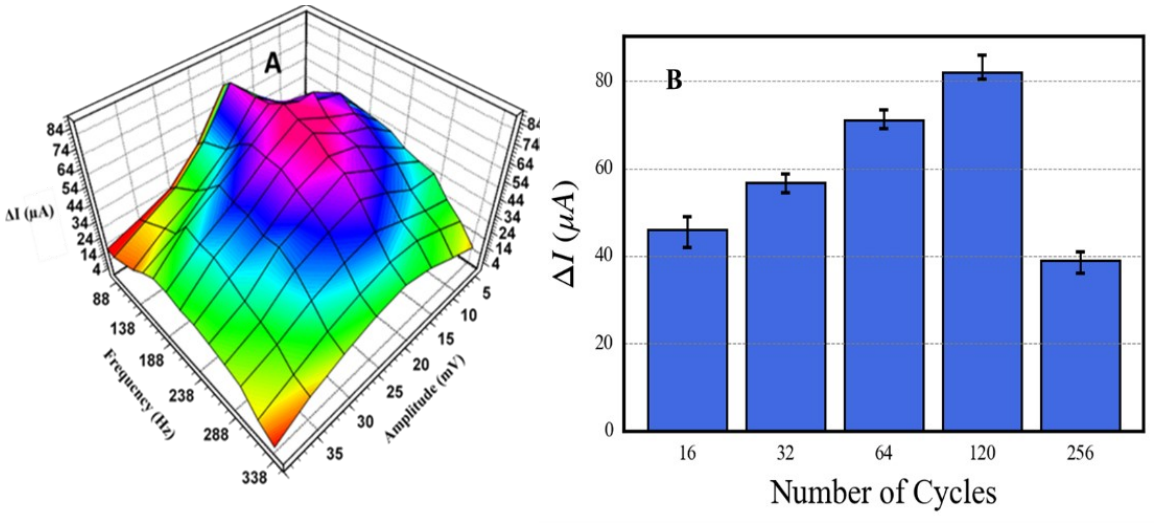

Figure S7. (A) The effect of the Frequency/amplitude and (B) cycles number on the electrode response after incubating in PBS pH 7.5, using FFTAV on the FFT-SWV response of the aptasensor. FFTSWV measurements were performed in 0.1 M KCl electrolyte PBS solution, pH 7.5 containing 5mM $[Fe(CN)_6]^{3-}$ redox , and presence of 1.0×10^3 PFU $mL^{-1}$of H9N2.

SI-5. Molecular docking

Supplementary Table S2 lists the hydrogen-bond interactions identified in the docked B4–protein complex, including interacting aptamer nucleotides, protein residues, and hydrogen-bond distances calculated from the docking simulations.

Table S-1. Detailed protein–aptamer interaction pairs for four representative aptamers (B4, A6, A21, and B25), showing receptor residue, ligand residue, and their interaction distance (in Å). Interactions within hydrogen bond distance (2.0–3.5 Å) are bolded to highlight specific hydrogen bonding events.

B4			**A6**			**A21**			**B25**		
RECEPTOR RESIDUE	LIGAND RESIDUE	DISTANCE	RECEPTOR RESIDUE	LIGAND RESIDUE	DISTANCE	RECEPTOR RESIDUE	LIGAND RESIDUE	DISTANCE	RECEPTOR RESIDUE	LIGAND RESIDUE	DISTANCE
GLU31A	DG26	3.801	LEU19A	DG22	4.538	LEU19A	DC22	3.971	LYS260	DG26	4.689

	S			S			S		A	S	
LEU33A	DG26 S	4.897	GLU100 A	DT9S	3.597	GLU100 A	DG8S	4.692	GLU275 A	DC24 S	4.053
HIS34A	**DG27 S**	**2.693**	GLU100 A	DT10S	4.77	**GLU100 A**	**DG9S**	**2.424**	GLU275 A	DG25 S	4.031
HIS34A	DC28 S	4.7	SER103 A	DT9S	3.957	SER103 A	DG8S	4.986	ARG276 A	DC24 S	4.142
SER36A	DG26 S	4.189	**LEU104 A**	**DC8S**	**3.447**	SER103 A	DG9S	3.903	ASN287 A	DT23S	3.964
SER36A	DG27 S	4.954	SER107 A	DT9S	4.609	LEU104 A	DG8S	3.89	ASN287 A	DC24 S	4.739
HIS37A	DT21S	3.844	**GLU197 A**	**DG4S**	**2.927**	SER107 A	DG9S	4.868	VAL288 A	DC24 S	4.064
GLN271 A	DG29 S	3.83	GLU197 A	DG5S	3.988	GLU197 A	DT4S	4.941	SER289 A	DC24 S	3.896
ARG276 A	DG19 S	4.666	ASP198 A	DG4S	3.947	**GLU197 A**	**DG5S**	**3.174**	**LYS290 A**	**DC24 S**	**3.446**
ARG276 A	**DG20 S**	**2.573**	ASP198 A	DG5S	3.681	ASP198 A	DT4S	3.921	**LYS290 A**	**DG25 S**	**3.169**
ARG276 A	**DT21S**	**2.546**	**ASP198 A**	**DG6S**	**2.259**	**ASP198 A**	**DG5S**	**2.396**	TYR291 A	DC24 S	4.32
ASN280 A	DG27 S	4.909	ILE199A	DG3S	4.994	**ASP198 A**	**DC6S**	**2.966**	**TYR291 A**	**DG25 S**	**2.113**
ASN280 A	**DC28 S**	**3.161**	ILE199A	DG4S	4.251	ILE199A	DG5S	4.89	TYR291 A	DG26 S	4.065
ASN280 A	**DG29 S**	**2.366**	ILE199A	DG5S	4.763	ASN200 A	DT1S	1.914	TYR299 A	DT23S	1.706
ASN280 A	DC30 S	3.919	ASN200 A	DC1S	1.818	**ASN200 A**	**DC2S**	**3.395**	TYR299 A	DC24 S	3.739
THR281 A	DG27 S	3.571	**ASN200 A**	**DG2S**	**3.273**	ASN200 A	DA3S	4.766	VAL300 A	DT23S	4.978
THR281 A	**DC28 S**	**3.245**	ASN200 A	DG3S	4.633	ARG201 A	DT1S	4.464	**GLY301 A**	**DT22S**	**2.151**
THR281 A	DG29 S	4.368	ARG201 A	DC1S	4.732	**THR202 A**	**DT1S**	**2.669**	**GLY301 A**	**DT23S**	**2.57**

THR282 A	DG27 S	4.948	**THR202 A**	**DC1S**	**3.407**	**LYS228 A**	**DG5S**	**3.495**	VAL302 A	DA21S	4.149
THR282 A	**DC28 S**	**2.903**	VAL226 A	DG6S	4.666	**LYS228 A**	**DC6S**	**2.998**	**VAL302 A**	**DT22S**	**3.294**
THR282 A	**DG29 S**	**3.483**	LYS228 A	DG5S	3.632	LYS228 A	DC7S	4.404	VAL302 A	DT23S	4.409
LEU283 A	DG26 S	4.627	LYS228 A	DG6S	3.945	GLN231 A	DG5S	4.433	LYS303 A	DT22S	4.345
LEU283 A	DG27 S	3.697	LYS228 A	DT7S	4.163	GLU253 A	DG9S	4.563	**LYS303 A**	**DT23S**	**3.486**
ASN287 A	DG19 S	4.575	GLN231 A	DG5S	4.364	PHE3B	DC29 S	4.265	LYS51B	GG13 S	4.6
ASN287 A	DG20 S	4.689	GLU253 A	DT9S	4.089	PHE3B	DC30 S	4.423	ASN54B	GG13 S	4.791
VAL288 A	DG20 S	3.576	PHE3B	DC29 S	4.004	LYS58B	DA18S	4.922	ASN54B	GG14 S	3.894
TYR299 A	**DG19 S**	**3.313**	PHE3B	DC30 S	4.144	**LYS58B**	**DT19S**	**3.049**	ILE55B	GG14 S	4.167
GLY301 A	**DG18 S**	**3.044**	LYS58B	DG19 S	3.873	**MET59B**	**DT19S**	**2.788**	LYS58B	GG13 S	4.821
GLY301 A	**DG19 S**	**3.348**	LYS58B	DG20 S	4.564	**MET59B**	**DC20 S**	**3.533**	**LYS58B**	**GG14 S**	**2.65**
VAL302 A	DG18 S	4.008	**MET59B**	**DG19 S**	**3.395**	HIS68B	DG9S	4.215	**LYS58B**	**GC15 S**	**3.053**
VAL302 A	DG19 S	4.704	MET59B	DG20 S	3.645	**HIS68B**	**DT10S**	**2.844**	MET59B	GC15 S	4.542
LYS303 A	DG18 S	3.896	HIS68B	DT9S	4.395	PHE70B	DT10S	4.263	ASP67B	DG25 S	4.899
LYS303 A	**DG19 S**	**3.305**	HIS68B	DT10S	3.946	**LEU77B**	**DT10S**	**2.946**	ASP67B	DG26 S	4.04
NAG1D	**DG29 S**	**2.48**	PHE70B	DT10S	4.585	LEU77B	DT11S	3.7	GLU72B	DT27S	4.958
NAG1D	DC30 S	1.743	**LEU77B**	**DT10S**	**3.278**	ILE80B	DT11S	4.209	GLU72B	DT28S	4.39
NAG1D	DC31	3.993	LEU77B	DG11	3.925	**ASN81B**	**DT10S**	**3.458**	THR75B	DT27S	4.154

	S			S							
NAG2D	**DC30 S**	**2.942**	ILE80B	DG11 S	4.61	**ASN81B**	**DT11S**	**3.135**	ASN78B	DG26 S	4.622
NAG2D	DC31 S	3.648	ASN81B	DT10S	4.305	**ILE84B**	**DT11S**	**2.67**	MET79B	DG26 S	4.51
NAG1E	DG18 S	4.696	ASN81B	DG11 S	3.817	ILE84B	DT12S	4.629	**ASN82B**	**DG25 S**	**3.357**
NAG1E	**DG19 S**	**2.285**	ILE84B	DG11 S	4.014	TRP92B	DA18S	4.41	**ASN82B**	**DG26 S**	**2.888**
NAG1E	DG20 S	1.466	ILE84B	DC12 S	4.382	TRP92B	DT19S	3.574	ASP85B	DG25 S	4.534
NAG1E	DT21S	4.645	ILE91B	DG19 S	4.915	TYR94B	DC20 S	3.64	ASP86B	DC24 S	4.875
NAG1E	DG23 S	4.751	TRP92B	DG19 S	3.523	**TYR94B**	**DG21 S**	**2.341**	ASP86B	DG25 S	3.973
NAG2E	DG20 S	4.202	TYR94B	DG20 S	4.616	ASN95B	DT19S	3.728	GLN87B	GC19 S	3.567
NAG2E	**DT21S**	**2.345**	**TYR94B**	**DC21 S**	**2.452**	ASN95B	DC20 S	4.194	GLN89B	DA21S	4.21
NAG2E	DG22 S	1.988	ASN95B	DG19 S	3.82	LEU98B	DC20 S	4.388	GLN89B	DT22S	3.517
NAG2E	**DG23 S**	**2.46**	ASN95B	DG20 S	3.897	LEU98B	DG21 S	3.582	**GLN89B**	**DT23S**	**2.553**
NAG2E	DG24 S	4.413	LEU98B	DC21 S	4.114	**LEU99B**	**DC20 S**	**3.449**	GLN89B	DC24 S	3.762
NAG2E	DT25S	4.624	**LEU99B**	**DG20 S**	**2.917**	LEU99B	DG21 S	3.521	ASP90B	GC19 S	4.056
			LEU99B	DC21 S	3.913	LEU102 B	DG21 S	3.887	**ASP90B**	**GG20 S**	**2.442**
			LEU102 B	DC21 S	3.588	**LEU102 B**	**DC22 S**	**3.267**	**ASP90B**	**DA21 S**	**3.279**
			LEU102 B	**DG22 S**	**2.42**	LYS106 B	DG21 S	4.078	**ASP90B**	**DT22S**	**3.324**
			LYS106 B	DC21 S	3.905	ASN116 B	DC30 S	1.925	ASP90B	DT23S	4.89

			ASN116 B	DC30 S	1.833	ASN116 B	DC31 S	3.875	ILE91B	GG17 S	4.534
			ASN116 B	DG31 S	3.597	ASN117 B	DC29 S	3.845	**ILE91B**	**GG18 S**	**2.862**
			ASN117 B	DC29 S	4.168	ASN117 B	DC30 S	4.101	ILE91B	GC19 S	4.205
			ASN117 B	DC30 S	3.538	**ASN120 B**	**DC30 S**	**2.959**	ILE91B	GG20 S	4.515
			ASN120 B	**DC30 S**	**3.104**	ASN120 B	DC31 S	3.913	TRP92B	GC15 S	4.676
			ASN120 B	DG31 S	3.6	LYS123 B	DC31 S	4.84	**TRP92B**	**TT16S**	**3.151**
			LYS123 B	DG31 S	4.944	**ARG124 B**	**DC30 S**	**3.018**	THR93B	GG20 S	4.492
			LYS123 B	DA32S	4.575				**THR93B**	**DA21 S**	**2.325**
			ARG124 B	**DC30 S**	**2.989**				THR93B	DT22S	4.345
			ARG124 B	DG31 S	4.632				TYR94B	GG17 S	4.681
									TYR94B	**GG18 S**	**3.127**
									TYR94B	**GC19 S**	**3.351**
									TYR94B	**GG20 S**	**3.059**
									TYR94B	DA21S	4.656
									ASN95B	TT16S	4.964
									ASN95B	GG17 S	4.742
									ASN95B	GG18 S	4.503
									GLU97B	**GG20 S**	**3.518**
									GLU97B	**DA21**	**2.877**

										S	
									LEU98B	GG20 S	4.508
									LEU99B	GG13 S	4.668
									LEU99B	GG14 S	3.731
									GLU103 B	**TT12S**	**3.18**
									GLU103 B	GG13 S	0.742
									LYS106 B	TT11S	4.999
									LYS106 B	**TT12S**	**2.729**
									LYS106 B	**GG13 S**	**2.244**

1. Heidari, N., et al., *A novel label-free immunosensor for detection of VEGF using FFT admittance voltammetry.* Bioelectrochemistry, 2025. **165**: p. 108948.
2. Ebrahimi, M., et al., *Advancing chirality analysis through enhanced enantiomer characterization and quantification via fast Fourier transform capacitance voltammetry.* Scientific Reports, 2023. **13**(1): p. 16739.
3. Gavaghan, D.J., et al., *Analysis of ramped square-wave voltammetry in the frequency domain.* Journal of Electroanalytical Chemistry, 2001. **512**(1-2): p. 1-15.
4. Jakubowska, M., *Signal processing in electrochemistry.* Electroanalysis, 2011. **23**(3): p. 553-572.